



# Boosting the internal electron transfer of two-dimensional hybrid perovskites via fluorination of organic cation towards enhanced photocatalytic hydrogen production

Jiaqi Liu<sup>a</sup>, Hefeng Zhang<sup>a</sup>, Junhui Wang<sup>b</sup>, Yuxin Xie<sup>c</sup>, Yuying Gao<sup>c</sup>, Chenghua Sun<sup>d,\*</sup>, Lianzhou Wang<sup>e,\*</sup>, Xu Zong<sup>a,\*</sup>

<sup>a</sup> Marine Engineering College, Dalian Maritime University, Linghai Road 1, Dalian 116026, China

<sup>b</sup> State Key Laboratory of Molecular Reaction Dynamics, Dalian Institute of Chemical Physics, Chinese Academy of Sciences, Dalian, Liaoning 116023, China

<sup>c</sup> State Key Laboratory of Catalysis, Dalian Institute of Chemical Physics, Chinese Academy of Sciences, Dalian National Laboratory for Clean Energy, Dalian 116023, China

<sup>d</sup> Department of Chemistry and Biotechnology, Swinburne University of Technology, Hawthorn, VIC 3122, Australia

<sup>e</sup> Nanomaterials Centre, School of Chemical Engineering and Australian Institute for Bioengineering and Nanotechnology, The University of Queensland, QLD 4072, Australia

## ARTICLE INFO

### Keywords:

Photocatalysis

Organic-inorganic hybrid perovskite

Two-dimensional

Hydrogen

Internal charge transfer

## ABSTRACT

Two-dimensional (2D) organic-inorganic hybrid perovskites have emerged as promising candidates for photocatalytic hydrogen production due to their unique optoelectronic properties. However, the organic cations in the interlayer of 2D perovskites generally retard the internal charge transfer due to the large interlayer van der Waals barrier for electron transfer, which defines the imperative to engineering the organic entity. Herein, taking phenethylammonium lead iodide (PEA<sub>2</sub>PbI<sub>4</sub>) as a typical example, we show that by substituting the hydrogen with fluorine atom in the para-position of the phenyl group, the internal electron transfer was promoted remarkably. The improved electron transfer is ascribed to the introduction of fluorine with strong electronegativity, which leads to interlayer polarization and almost zero-potential barrier between the organic layers. Consequently, 4-FPEA<sub>2</sub>PbI<sub>4</sub> exhibits *ca.* 8.2 times higher photocatalytic H<sub>2</sub> evolution activity than PEA<sub>2</sub>PbI<sub>4</sub>. This work establishes a paradigm for optimizing the photocatalytic properties of 2D hybrid perovskites by engineering the organic cations.

## 1. Introduction

Producing green hydrogen (H<sub>2</sub>) fuel with solar energy has been proposed as a promising approach to address the global energy and environmental problems [1–3]. Photocatalytic H<sub>2</sub> production on semiconductor materials from different sources like water, organic compounds, pollutants, and hydrohalic acids has been regarded as an ideal way to convert and store solar energy in the form of hydrogen fuel [4–6]. As semiconductor-based photocatalysts are the main carrier for driving photocatalytic H<sub>2</sub> production reactions [7–11], identifying efficient photocatalyst has always been the research focus in this field.

Organic-inorganic hybrid perovskites (OHPs) exhibit excellent optoelectronic properties and have emerged as potential platform for producing hydrogen fuel [12–14]. Although the instability issue of OHPs

in aqueous solution has been originally deemed to be an insurmountable obstacle for their applications in aqueous solution, this issue has been ingeniously addressed by Park and his colleagues. They showed that three-dimensional (3D) perovskite methylammonium lead iodide (MAPbI<sub>3</sub>) can be stabilized in saturated aqueous solution through establishing dissolution-reprecipitation equilibrium, and the as-stabilized MAPbI<sub>3</sub> can realize visible-light-driven photocatalytic H<sub>2</sub> evolution reaction [15]. Similar strategy has been extended to stabilizing other perovskites for photocatalytic H<sub>2</sub> production reactions [16–18]. However, the serious recombination of photogenerated charges in perovskites seriously limit their photocatalytic activities. Therefore, different strategies like hybridization strategy [17,19,20], electronic structure engineering [18] and the loading of co-catalysts [21–27] have been employed to improve the charge separation and

\* Corresponding authors.

E-mail addresses: [chenghuasun@swin.edu.au](mailto:chenghuasun@swin.edu.au) (C. Sun), [l.wang@uq.edu.au](mailto:l.wang@uq.edu.au) (L. Wang), [xuzong@dlmu.edu.cn](mailto:xuzong@dlmu.edu.cn) (X. Zong).

<https://doi.org/10.1016/j.apcatb.2024.124018>

Received 6 December 2023; Received in revised form 13 March 2024; Accepted 29 March 2024

Available online 1 April 2024

0926-3373/© 2024 Elsevier B.V. All rights reserved.

transfer processes.

Besides 3D perovskites, two-dimensional (2D) perovskites were recently identified to be potential candidate for driving efficient photocatalytic hydrogen production reaction [28]. Compared with the 3D counterparts, 2D perovskites exhibit unique structural as well as physicochemical properties like improved moisture resistance [29], greatly enhanced photostability and thermal stability [30] and significantly reduced ion mobility [31]. In recent years, 2D perovskites have gained extensive attention in the various fields like photovoltaics, photodetectors, light-emitting diodes and catalysis [32–36]. 2D perovskites consist of inorganic layers of corner-sharing  $[MX_6]^{4-}$  octahedra confined between interdigitating bilayers of long chain alkylammonium cations. The inorganic and organic layers are stacked together by a combination of Coulombic and hydrophobic forces, which maintain the structural integrity [37,38]. The electronic structure of 2D perovskites can be regarded as quantum wells, in which the semiconductor inorganic layer acts as "wells" and the insulating organic layer acts as "barriers" [39]. Furthermore, the quantum well structure and optoelectronic properties of 2D perovskites can be finely tuned by varying the layer thickness, the cage cation and the spacer cation, which is conducive to the optimization of the optoelectronic properties [40].

Considering the attractive properties of 2D perovskites, we first employed a series of phenylalkylammonium 2D perovskites as photocatalysts for driving photocatalytic  $H_2$  evolution reaction [28]. However, the bulky organic cations in the interlayer of 2D perovskites generally retard the interlayer and therefore the internal electron transfer due to the large interlayer van der Waals barrier, which impairs their photocatalytic performance. We hypothesize that the internal charge separation/transfer processes of 2D perovskites could be improved towards enhanced photocatalytic activity by rationally engineering the organic cations in the interlayer, which has been rarely reported in the field of hybrid perovskite-based photocatalysis.

It has been reported that the fluorination of organic spacer cations can influence the crystal and electronic structures of perovskites [41–43]. For example, in the field of perovskite solar cells, the fluorination of organic functional groups has been shown to be effective in modifying the energy levels of perovskites, improving film morphology, and increasing the power conversion efficiency of organic solar cells [44, 45]. Moreover, the employment of fluorinated organic cations as a spacer can improve the stability of perovskite solar cells [46,47]. In the field of thin-film transistors, fluorine substitution on the organic cation of perovskite was found to be capable of modifying the crystal structures and enhancing bulky molecules interaction between the perovskite frameworks, resulting in different transport properties [48–50]. We suppose that by engineering the organic spacer cations with fluorination strategy, we can tune the charge transport properties of perovskites and improve the photocatalytic  $H_2$  production performance. However, to the best of our knowledge, work on employing fluorinated perovskites for photocatalytic  $H_2$  production reactions has not been reported.

For fluorination, it can occur at different positions of the organic functional groups. Taking phenethylammonium lead iodide ( $PEA_2PbI_4$ ) as an example, fluorine substitution can occur at the ortho, meta and para positions of the phenethylammonium (PEA) organic cation, which are described as 2-FPEA $_2PbI_4$ , 3-FPEA $_2PbI_4$  and 4-FPEA $_2PbI_4$ , respectively. Among these three perovskites, 4-FPEA $_2PbI_4$  exhibits the most ordered structure and highest formation energy [43,51–55]. Therefore, 4-FPEA $_2PbI_4$  could hold great promise for more efficient photocatalysis.

Herein, we showed that the substitution of the hydrogen with fluorine atom in the para-position of the phenyl group of  $PEA_2PbI_4$  can promote the internal electron transfer process and therefore significantly enhance the photocatalytic hydrogen evolution activity. Transient absorption spectra (TA), Kelvin probe force microscopy (KPFM) together with density functional theory (DFT) calculations testified that fluorine, due to its strongest electronegativity, played crucial roles in modifying the geometries of the parent  $PEA_2PbI_4$ , introducing strong interlayer polarization and effectively reducing electron potential

barrier when photo-induced electrons transfer along the direction vertical to Pb-I-Pb plane. Consequently, the resulting 4-FPEA $_2PbI_4$  exhibits drastically enhanced photocatalytic  $H_2$  evolution activity compared with the parent  $PEA_2PbI_4$ .

## 2. Experimental section

### 2.1. Chemicals and materials

$PbI_2$  (99.999%), phenethylamine (99%), 4-fluorophenethylamine (99%),  $H_2PtCl_6 \cdot 6H_2O$ , DMSO, and DMF were purchased from Sigma Aldrich. HI (57 wt%, unstabilized) and  $H_3PO_2$  (50 wt%, in water) were purchased from Macklin. Diethyl ether was received from Sinopharm Chemical Reagent Co., Ltd. These chemicals and reagents were used as received without further purification.

### 2.2. Materials synthesis

#### 2.2.1. Synthesis of iodine salt

Phenethylammonium iodide is synthesized by adding 10 mL phenethylamine (4-fluorophenethylamine) to 10 mL ethanol and then cooling the solution in an ice bath. 20 mL of HI solution is added dropwise over several minutes. The reaction was allowed to proceed for 1 h at ice bath under ambient conditions. Then the precipitates were subsequently washed by diethyl ether and recrystallized in isopropanol. The final products were dried under vacuum at 40 °C overnight.

#### 2.2.2. Synthesis of 2D perovskite powders

To fabricate 2D perovskite powders, 0.461 g  $PbI_2$  and 0.498 g PEA $I$  or 0.534 g 4-FPEA $I$  dissolved in 5 mL HI/ $H_3PO_2$  (4 mL for HI and 1 mL for  $H_3PO_2$ ) mix solution. The solution was heated at 100 °C until completely dissolved into a bright yellow transparent solution. Then the solution was cooled to room temperature to obtain 2D perovskite precipitates. The 2D perovskite precipitates were separated from the saturated solution by a centrifuge treatment and dried under vacuum at 60 °C for 48 h. The 2D perovskite powders were used in photocatalytic  $H_2$  evolution reactions.

#### 2.2.3. Fabrication of 2D perovskite and Pt/2D perovskites films

2D perovskites and Pt/2D perovskite films were used for time-resolved photoluminescence (TRPL) and transient absorption (TA) measurements. 2D perovskites and Pt/2D perovskites films were prepared on quartz. The quartz was sequentially washed with 2 M KOH and deionized water for 10 min with sonication. A platinum disk (99.99% purity, 0.2 mm thickness, 60 mm diameter.) was used as the target. The Pt was deposited on quartz with the power of 66 W for 3 s. The precursor solution was prepared by dissolving 0.461 g  $PbI_2$  and 0.461 g PEA $I$  or 0.478 g 4-FPEA $I$  in 1 mL mixed solvent of DMF and DMSO (volume ratio of 4:1). 30  $\mu$ L of precursor solution was spin-coated onto the quartz or Pt/quartz substrate, and then the sample was spun at 3000 r.m.p for 30 s, followed by annealing at 100 °C in air for 10 min.

### 2.3. Photocatalytic $H_2$ evolution reaction

Photocatalytic  $H_2$  evolution was performed in a top-irradiation vessel, which is connected to a glass-enclosed gas circulation system. A 300 W Xe-lamp (Perforct Light, PLS-SXE 300) with a 420 nm cut-off filter was used as a visible light source for photocatalytic  $H_2$  evolution. A 15 mL aqueous solution containing 1.5 mL  $H_3PO_2$  was adopted, and 1.865 g PEA $I$  or 2.000 g 4-FPEA $I$  was used as the stabilizer reagent for photocatalytic reaction. 50 mg 2D perovskite powder was successively added to the solution. Then, a certain amount of  $H_2PtCl_6$  solution (calculated as Pt metal) was added to the solution. The temperature of the reaction system was maintained at 5 °C by circulating cooling water. The  $H_2$  evolved from the reaction was analyzed by gas chromatography (Tianmei, GC-7900) using Ar as the carrier gas.

To optimize the hydrogen evolution performance of 4-FPEA<sub>2</sub>PbI<sub>4</sub>, we tested the hydrogen evolution activity of perovskites loaded with different co-catalysts, and the test procedure is as follows. First, a 5 mL aqueous solution containing 0.5 mL H<sub>3</sub>PO<sub>2</sub> was adopted, and 3.73 g PEA<sub>2</sub>PbI<sub>4</sub> or 3.99 g 4-FPEA<sub>2</sub>PbI<sub>4</sub> was used as the stabilizer reagent for photocatalytic reaction. After that, 10 mg of 2D perovskite powders and different noble metal co-catalysts were sequentially added to the reaction solution with constant stirring. Photocatalytic reactions were performed in a home-made reactor. A 300 W Xe-lamp (Perfort Light, PLS-SXE 300) with a 420 nm cut-off filter was used as a visible light source for the photocatalytic reaction. The reaction system was purged with Ar three times to remove the air inside before irradiation. The amount of evolved H<sub>2</sub> from the reaction was determined by gas chromatography (Shimadzu, GC-2014 C) with Ar as the carrier gas.

The quantum yield is calculated from the ratio of the number of reacted electrons during the hydrogen evolution to the number of incident photons according to the following equation:

$$\text{Quantum yield} = \frac{2 \times \text{the number of evolved hydrogen molecules}}{\text{the number of incident photons}} \times 100\%$$

#### 2.4. Material characterizations

The as-prepared perovskite samples were characterized by X-ray power diffraction (XRD) on a Rigaku D/Max-2500/PC powder diffractometer using Cu-K $\alpha$  radiation at an operating voltage of 40 kV and a current of 200 mA, with a scan step of 2 ° min<sup>-1</sup>. UV-Vis diffuse reflectance spectra were recorded on a UV-Vis spectrophotometer (Shimadzu, UV-2600) equipped with an integrating sphere, using 100% BaSO<sub>4</sub> as reflectance standard. The morphology of perovskite was studied by scanning electron microscopy (SEM) with Tescan VEGA3. Steady-state photoluminescence (PL) spectra and time-resolved photoluminescence (TRPL) spectra was obtained on Edinburgh fluorescence spectrometer (FLS920). The details of the ultraviolet photoelectron spectroscopy (UPS), Kelvin probe force microscopy (KPFM), transient absorption spectra (TA), and density functional theory (DFT) calculations were provided in SI.

### 3. Results and discussion

PEA<sub>2</sub>PbI<sub>4</sub> perovskite was synthesized according to a reported approach [28]. To tune the optoelectronic properties of PEA<sub>2</sub>PbI<sub>4</sub>, PEA in the interlayer of PEA<sub>2</sub>PbI<sub>4</sub> was modified by substituting the hydrogen

with fluorine atom in the para-position of the phenyl group. Fig. 1 shows the schematic geometries of PEA<sub>2</sub>PbI<sub>4</sub> and 4-FPEA<sub>2</sub>PbI<sub>4</sub>. Both 2D perovskites are consisted of sheets of corner-sharing [PbI<sub>6</sub>]<sup>4-</sup> octahedra that are separated by organic cations. However, for PEA<sub>2</sub>PbI<sub>4</sub> the PEA organic layers prefer to be stacked in an edge-to-face manner, while for 4-FPEA<sub>2</sub>PbI<sub>4</sub> the 4-FPEA organic layers are stacked in parallel [51]. Moreover, the packing of 4-FPEA<sub>2</sub>PbI<sub>4</sub> has the cations within the interlayer gallery facing the same direction in a co-aligned fashion, indicating that its structure is fully ordered [43].

The as-prepared PEA<sub>2</sub>PbI<sub>4</sub> and 4-FPEA<sub>2</sub>PbI<sub>4</sub> perovskites were first investigated with powder X-ray diffraction (XRD) characterization. As shown in Fig. 2a, all the diffraction peaks of the as-prepared samples can be well indexed to those of the standard samples [54]. Moreover, the diffraction peaks of 4-FPEA<sub>2</sub>PbI<sub>4</sub> were slightly shifted towards smaller angles compared to those of PEA<sub>2</sub>PbI<sub>4</sub>, indicating the increased distance between the inorganic layers in 4-FPEA<sub>2</sub>PbI<sub>4</sub> perovskite. It has been reported that the diameters of PEA and 4-FPEA are 10.55 and 11.05 Å, respectively [50]. This increase in the size of the organic cation should be attributed to the substitution of hydrogen by fluorine atom with larger ionic radius, which in turn leads to an increase in the interlayer distance of 4-FPEA<sub>2</sub>PbI<sub>4</sub> perovskite. Based on the (002) diffraction peaks, the interlayer distances of PEA<sub>2</sub>PbI<sub>4</sub> and 4-FPEA<sub>2</sub>PbI<sub>4</sub> perovskites were calculated to be ca. 16.4 and 16.7 Å, respectively.

We then employed UV-Vis diffuse reflectance spectroscopy to investigate the optical properties of the PEA<sub>2</sub>PbI<sub>4</sub> and 4-FPEA<sub>2</sub>PbI<sub>4</sub> perovskite crystals. As shown in Fig. 2b, the PEA<sub>2</sub>PbI<sub>4</sub> and 4-FPEA<sub>2</sub>PbI<sub>4</sub> perovskites exhibit absorption edges at ca. 560 and 565 nm, respectively. According to the Kubelka-Munk equation (Figure S1), the bandgaps of PEA<sub>2</sub>PbI<sub>4</sub> and 4-FPEA<sub>2</sub>PbI<sub>4</sub> are calculated to be ca. 2.22 and 2.21 eV, respectively. Therefore, the substitution of hydrogen with fluorine atom in the para position of the PEA cation can only result in negligible change in the bandgap.

The morphological features of the as-prepared 2D perovskites were then characterized with scanning electron microscopy (SEM). As shown in Fig. 2c-d, both PEA<sub>2</sub>PbI<sub>4</sub> and 4-FPEA<sub>2</sub>PbI<sub>4</sub> perovskite crystals exhibit a plate-like morphology with similar dimensions and a typical layered structure. Moreover, energy dispersive spectrometry (EDS) elemental mapping (Figure S2) indicates the presence and uniform distribution of F, C, N, Pb and I elements in 4-FPEA<sub>2</sub>PbI<sub>4</sub>. These facts indicate that the substitution of hydrogen with fluorine atom in the para position of PEA cation does not significantly affect the morphology of the 2D perovskites.

As both PEA<sub>2</sub>PbI<sub>4</sub> and 4-FPEA<sub>2</sub>PbI<sub>4</sub> perovskites exhibit strong light

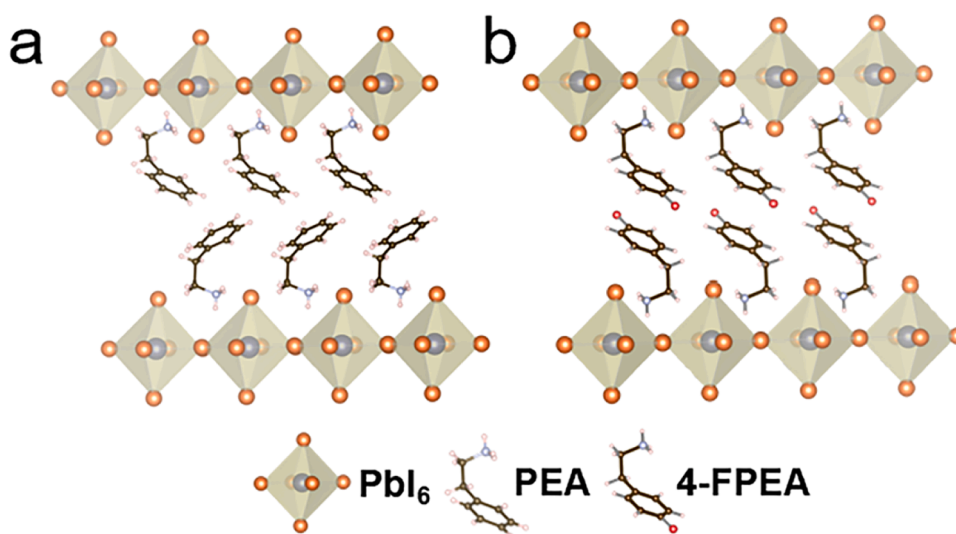


**Fig. 1.** The schematic geometries of 2D perovskites. (a) PEA<sub>2</sub>PbI<sub>4</sub>, and (b) 4-FPEA<sub>2</sub>PbI<sub>4</sub>. Basic inorganic unit PbI<sub>6</sub> is shown as the transparent octahedrons, together with organic links PEA between PbI<sub>6</sub> units. F and H terminals are shown as red and grey balls.

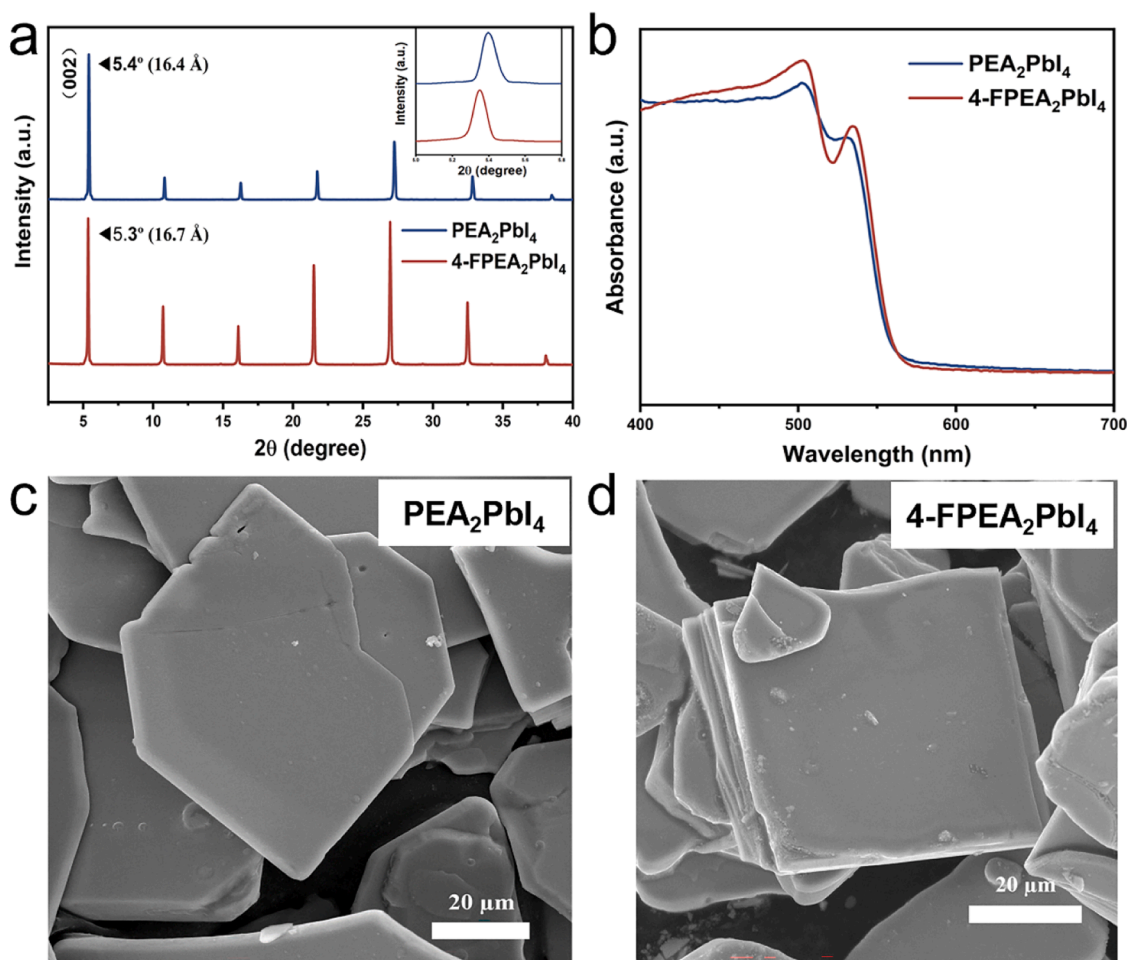


**Fig. 2.** (a) XRD patterns, (b) UV-Vis diffuse reflectance spectra, and (c-d) SEM images of PEA<sub>2</sub>PbI<sub>4</sub> and 4-FPEA<sub>2</sub>PbI<sub>4</sub> perovskite powders.

absorption in the visible region, we tentatively employed these 2D perovskite crystals as photocatalysts for H<sub>2</sub> evolution reaction in aqueous solution under visible light irradiation ( $\lambda > 420$  nm). The first key step of using 2D perovskites to drive photocatalytic H<sub>2</sub> evolution reaction is to stabilize them in aqueous solution although 2D perovskites are more tolerant to moisture than the 3D counterparts. A number of studies have shown that hybrid perovskites can be stabilized in saturated HI solution through establishing dissolution-reprecipitation equilibrium since the pioneering work by Park et al. [35]. Similarly, this dissolution-reprecipitation equilibrium mechanism can be applied to stabilizing 2D perovskites in aqueous solution. We showed in our previous studies that PEA<sub>2</sub>PbI<sub>4</sub> can be stabilized in PEA<sub>2</sub>I aqueous solution when the concentration of PEA<sub>2</sub>I is higher than 0.3 M. Following such success [8], we tentatively stabilized 4-FPEA<sub>2</sub>PbI<sub>4</sub> in aqueous solution by tuning the concentration of the corresponding iodine salts in aqueous solution. We found that the 4-FPEA<sub>2</sub>PbI<sub>4</sub> perovskite can also be stabilized in aqueous solution that contains the corresponding iodine salts with concentration higher than 0.3 M (Figure S3). Subsequently, the as-stabilized 4-FPEA<sub>2</sub>PbI<sub>4</sub> can be potentially used as photocatalysts for photocatalytic hydrogen evolution.

After the successful stabilization of PEA<sub>2</sub>PbI<sub>4</sub> and 4-FPEA<sub>2</sub>PbI<sub>4</sub> in aqueous solution, the photocatalytic H<sub>2</sub> evolution performance of these 2D perovskites were evaluated in aqueous solution containing the corresponding iodine salts. As shown in Fig. 3a, the rate of H<sub>2</sub> evolution on bare PEA<sub>2</sub>PbI<sub>4</sub> was ca. 1.6  $\mu\text{mol h}^{-1}$ . As for 4-FPEA<sub>2</sub>PbI<sub>4</sub>, the rate of hydrogen evolution was ca. 14.6  $\mu\text{mol h}^{-1}$  under the same reaction conditions, which is ca. 9.2 times of that obtained on PEA<sub>2</sub>PbI<sub>4</sub>. To further promote the photocatalytic activities of the 2D perovskites, Pt

was deposited as the H<sub>2</sub> evolution reaction co-catalyst with an in-situ reduction method. X-Ray photoelectron spectroscopy (XPS) analysis indicates that the as-deposited Pt exists in a chemical state of both zero and plus two (Figure S4) [56–59]. After depositing 0.5 wt% of Pt, the rate of hydrogen evolution on PEA<sub>2</sub>PbI<sub>4</sub> was drastically increased to ca. 42.8  $\mu\text{mol h}^{-1}$ . As for 4-FPEA<sub>2</sub>PbI<sub>4</sub>, the rate of H<sub>2</sub> evolution was enhanced to ca. 88.6  $\mu\text{mol h}^{-1}$  after depositing 0.5 wt% Pt, which is ca. 2.07 times of that obtained on 0.5 wt% Pt/PEA<sub>2</sub>PbI<sub>4</sub> (Fig. 3b). Therefore, the para-fluorine substitution on PEA organic cation can significantly enhance the photocatalytic hydrogen evolution activities of the 2D PEA<sub>2</sub>PbI<sub>4</sub> perovskite in the absence or presence of Pt co-catalyst.

As drastically enhanced photocatalytic hydrogen evolution activities were obtained on 4-FPEA<sub>2</sub>PbI<sub>4</sub>, we tentatively optimized its activity by tuning the amount and the type of the as-deposited co-catalysts. As shown in Fig. 3c, the rate of hydrogen evolution on 4-FPEA<sub>2</sub>PbI<sub>4</sub> increased from ca. 14.6 to ca. 33.51  $\mu\text{mol h}^{-1}$  after depositing 0.1 wt% Pt as the co-catalyst. By increasing the amount of Pt, the rate of hydrogen evolution on Pt/4-FPEA<sub>2</sub>PbI<sub>4</sub> gradually increased. A maximum value of ca. 88.6  $\mu\text{mol h}^{-1}$  was obtained at an optimum loading of 0.5 wt%. Further increase in the amount of Pt deposited led to slight decrease in the photocatalytic activity. The volcano-like relationship between the photocatalytic activity and the amount of deposited co-catalyst is ascribed to the compromise between the increased number of effective reaction sites for promoting hydrogen evolution and the reduced light absorption by 4-FPEA<sub>2</sub>PbI<sub>4</sub> perovskites due to light shading associated with Pt co-catalyst loading [60,61], in which effect has been widely observed with other noble metals as potential co-catalysts [62–67]. As shown in Figure S5, the rates of hydrogen



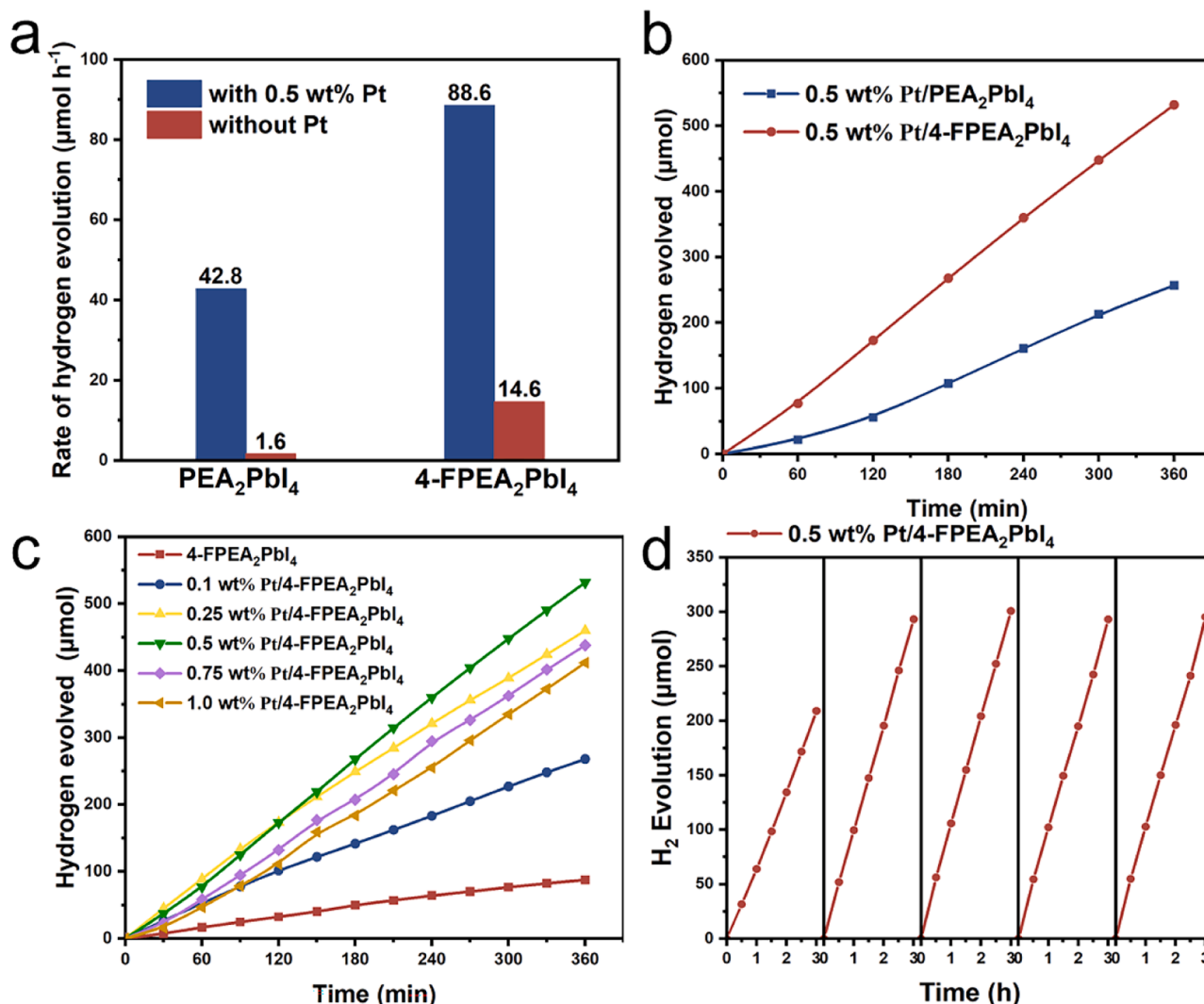


**Fig. 3.** (a) The rates of photocatalytic H<sub>2</sub> evolution on bare 2D perovskites and those deposited with Pt (0.5 wt%) co-catalyst. (b) Time courses of photocatalytic H<sub>2</sub> evolution on Pt (0.5 wt%)/PEA<sub>2</sub>PbI<sub>4</sub> and Pt (0.5 wt%)/4-FPEA<sub>2</sub>PbI<sub>4</sub>. (c) Time courses of photocatalytic H<sub>2</sub> evolution on Pt/4-FPEA<sub>2</sub>PbI<sub>4</sub> with different Pt loadings. (d) Cycling tests of photocatalytic hydrogen evolution on Pt (0.5 wt%)/4-FPEA<sub>2</sub>PbI<sub>4</sub> under visible light irradiation. Reaction conditions: 13.5 mL deionized water and 1.5 mL H<sub>3</sub>PO<sub>2</sub> with precursor iodine salt, 50 mg of perovskite photocatalyst, 300 W xenon lamp ( $\lambda > 420$  nm), reaction cell: top-irradiation cell with a Pyrex window.

evolution on 0.5 wt% Pt/4-FPEA<sub>2</sub>PbI<sub>4</sub>, 0.5 wt% Ir/4-FPEA<sub>2</sub>PbI<sub>4</sub>, 0.5 wt% Ru/4-FPEA<sub>2</sub>PbI<sub>4</sub>, and 0.5 wt% Rh/4-FPEA<sub>2</sub>PbI<sub>4</sub> were ca. 81.5, 25, 37 and 56.5  $\mu\text{mol h}^{-1}$ , respectively. Therefore, Pt was identified to be the best co-catalyst for promoting photocatalytic H<sub>2</sub> evolution on 4-FPEA<sub>2</sub>PbI<sub>4</sub>. Under the optimum conditions, a quantum yield of 2.4% at 420 nm is obtained on Pt (0.5 wt%)/4-FPEA<sub>2</sub>PbI<sub>4</sub> (Figure S6).

Besides evaluating the photocatalytic hydrogen production activities of PEA<sub>2</sub>PbI<sub>4</sub> and 4-FPEA<sub>2</sub>PbI<sub>4</sub>, we also tested their stability during cycling reactions. As shown in Figure S7, bare 4-FPEA<sub>2</sub>PbI<sub>4</sub> exhibits stable photocatalytic hydrogen evolution activity during cycling test. For Pt/PEA<sub>2</sub>PbI<sub>4</sub> and Pt/4-FPEA<sub>2</sub>PbI<sub>4</sub>, the amount of H<sub>2</sub> evolved in the first cycle is slightly lower than that observed in the next four cycles due to the photo-deposition of Pt co-catalyst in the first cycle (Fig. 3d, Figure S8). No decrease in the photocatalytic activities of Pt/PEA<sub>2</sub>PbI<sub>4</sub> and Pt/4-FPEA<sub>2</sub>PbI<sub>4</sub> is observed in the following four cycles, indicating their good stability under the testing conditions. Moreover, no notable changes in the XRD patterns (Figure S9), SEM images (Figure S10) and XPS (Figure S11) spectra for 4-FPEA<sub>2</sub>PbI<sub>4</sub> after photocatalytic hydrogen production reactions, which again demonstrates its good photochemical stability. Therefore, with the substitution of hydrogen with fluorine atom at the para-position of the PEA organic cation, the resulting 4-FPEA<sub>2</sub>PbI<sub>4</sub> exhibited much higher photocatalytic activity than the

parent PEA<sub>2</sub>PbI<sub>4</sub> while preserved the good stability. This inspired us to investigate the roles of the intercalated 4-FPEA cation played during the reaction.

We first analyzed the energy band structures of PEA<sub>2</sub>PbI<sub>4</sub> and 4-FPEA<sub>2</sub>PbI<sub>4</sub> perovskites with ultraviolet photoelectron spectroscopy (UPS). As shown in Fig. 4a, the secondary electron cut-off binding energy is ca. 16.5 and 16.0 eV, thus the work function ( $E_F$ , the difference between the energy of the incident photon (21.2 eV) and the secondary electron cut-off binding energy) of PEA<sub>2</sub>PbI<sub>4</sub> and 4-FPEA<sub>2</sub>PbI<sub>4</sub> is 4.7 and 5.2 eV, respectively. The relationship between the  $E_F$  and the vacuum level ( $E_{vac}$ ) is  $\Phi = E_{vac} - E_F$ , which means, the  $E_F$  of PEA<sub>2</sub>PbI<sub>4</sub> and 4-FPEA<sub>2</sub>PbI<sub>4</sub> with respect to vacuum level is ca. -4.7 and -5.2 eV, respectively [68]. The low binding energy edge of ca. 1.2 and 1.1 eV represents the difference between the  $E_F$  and the valence band maximum ( $E_V$ ,  $E_F - E_V = 1.2$  and 1.1 eV). Therefore, the  $E_V$  of PEA<sub>2</sub>PbI<sub>4</sub> and 4-FPEA<sub>2</sub>PbI<sub>4</sub> with respect to vacuum level is calculated to be -5.9 and -6.3 eV, respectively [69]. As the band gap of PEA<sub>2</sub>PbI<sub>4</sub> and 4-FPEA<sub>2</sub>PbI<sub>4</sub> is ca. 2.22 and 2.21 eV, respectively, the conduction band ( $E_C$ ) of these 2D perovskites can be inferred to be at ca. -3.7 and -4.1 eV, respectively. According to the relationship between vacuum level and normal hydrogen electrode (NHE) ( $E_{NHE}$  (V) = -4.5 -  $E_{vac}$  (eV)) [70], the  $E_V$  of PEA<sub>2</sub>PbI<sub>4</sub> and 4-FPEA<sub>2</sub>PbI<sub>4</sub> correspond to ca. 1.4

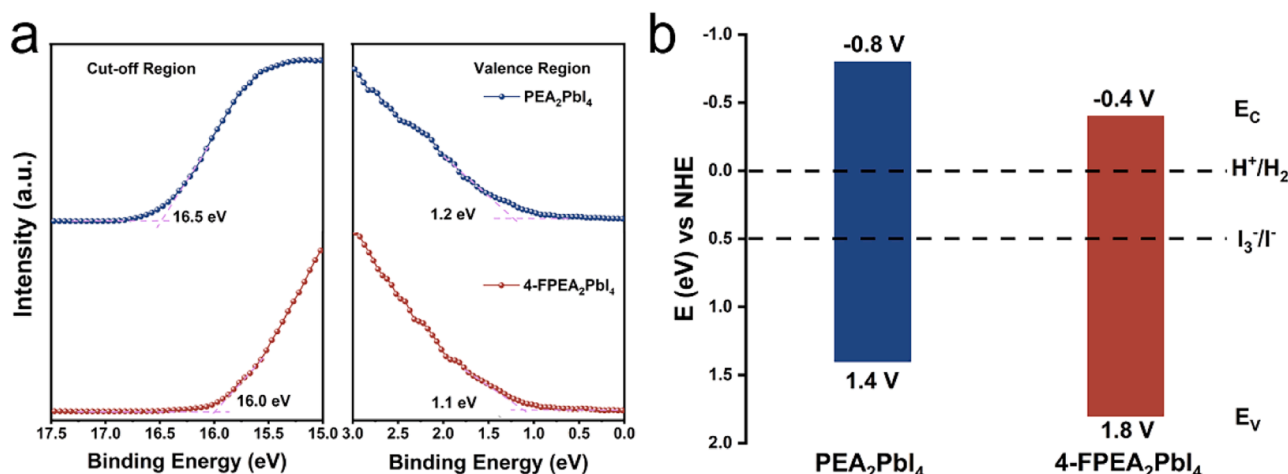


**Fig. 4.** (a) UPS spectra of PEA<sub>2</sub>PbI<sub>4</sub> and 4-FPEA<sub>2</sub>PbI<sub>4</sub> perovskites. (b) The schematic energy diagrams of PEA<sub>2</sub>PbI<sub>4</sub> and 4-FPEA<sub>2</sub>PbI<sub>4</sub> perovskites relative to the redox potentials of HI splitting reaction.

and 1.8 V versus NHE, the  $E_C$  of PEA<sub>2</sub>PbI<sub>4</sub> and 4-FPEA<sub>2</sub>PbI<sub>4</sub> correspond to ca. -0.8 V and -0.4 V versus NHE, respectively. Figure S12 illustrates the formula for calculating the energy bands of 2D perovskites. Based on the above analysis, the energy diagrams of PEA<sub>2</sub>PbI<sub>4</sub> and 4-FPEA<sub>2</sub>PbI<sub>4</sub> perovskites were schematically depicted in Fig. 4b. These results are in good agreement with those reported in previous work and indicate that the PEA<sub>2</sub>PbI<sub>4</sub> and 4-FPEA<sub>2</sub>PbI<sub>4</sub> perovskites fulfill the thermodynamic requirement for both proton reduction and I<sup>-</sup> oxidation reactions [43]. Moreover, as PEA<sub>2</sub>PbI<sub>4</sub> exhibited higher conduction band relative to that of 4-FPEA<sub>2</sub>PbI<sub>4</sub>, it is generally supposed to be more efficient for the proton reduction reaction. However, this trend in energy band structure is in contradiction with the results obtained from the photocatalytic H<sub>2</sub> evolution reaction tests. We speculate that as the conduction and valence bands of both PEA<sub>2</sub>PbI<sub>4</sub> and 4-FPEA<sub>2</sub>PbI<sub>4</sub> are much more energetic than the corresponding proton reduction and I<sup>-</sup> oxidation reactions, their difference in the energy levels will not be the main reason for the different photocatalytic activities. Therefore, more intrinsic factors regarding the influence of 4-FPEA cation on the photocatalytic performance of 4-FPEA<sub>2</sub>PbI<sub>4</sub> need to be clarified.

Generally, the carrier transfer dynamics are the most intrinsic factors that determine the performance of a photocatalyst. Therefore, steady-state photoluminescence (PL) spectroscopy, time-resolved photoluminescence (TRPL) spectroscopy and transient absorption (TA) spectroscopy analysis were then employed to compare the carrier dynamics of PEA<sub>2</sub>PbI<sub>4</sub> and 4-FPEA<sub>2</sub>PbI<sub>4</sub> perovskites. As shown in Figure S13, PEA<sub>2</sub>PbI<sub>4</sub> and 4-FPEA<sub>2</sub>PbI<sub>4</sub> perovskites exhibit PL peaks at ca. 528 and 529 nm, respectively, which correspond to the energy value of the excitonic peak in the UV-Vis absorption spectra. Moreover, the intensity of the PL peak of PEA<sub>2</sub>PbI<sub>4</sub> is higher than that of 4-FPEA<sub>2</sub>PbI<sub>4</sub>, indicating the decreased recombination of photogenerated carriers in 4-FPEA<sub>2</sub>PbI<sub>4</sub> perovskite [71,72]. The TRPL spectroscopy was then employed to gain more insight into the decay behavior of photo-generated carriers in the two perovskites. The resulting TRPL spectra were fitted with a bi-exponential decay model (Figure S14) and the average lifetime of PEA<sub>2</sub>PbI<sub>4</sub> and 4-FPEA<sub>2</sub>PbI<sub>4</sub> perovskites was determined to be ca. 740.5 and 406.0 ps, respectively. As smaller decay time corresponds to faster transfer of electrons, the TRPL analysis indicated that 4-FPEA<sub>2</sub>PbI<sub>4</sub> exhibited more efficient electron-hole separation and rapid charge transfer than the PEA<sub>2</sub>PbI<sub>4</sub> counterpart.

We then employed TA spectroscopy to further investigate the charge transfer dynamics of the 2D perovskites and Pt/perovskites due to its better time resolution that allows for more accurate extraction of electron and hole transfer time constant and efficiency. Detailed information on the TA set-ups can be found in SI and Figure S15. The TA spectra of PEA<sub>2</sub>PbI<sub>4</sub> and 4-FPEA<sub>2</sub>PbI<sub>4</sub> samples are dominated by an exciton bleach

featured at ~520 nm (Fig. 5a-d) and the exciton bleach kinetics for the bare perovskites are shown in Figure S16. The exciton bleach kinetics can be fitted as a bi-exponential decay model with an average life of ca. 528.5 and 359.0 ps for PEA<sub>2</sub>PbI<sub>4</sub> and 4-FPEA<sub>2</sub>PbI<sub>4</sub> perovskites, respectively (Table S1). The faster kinetic decay of 4-FPEA<sub>2</sub>PbI<sub>4</sub> indicates that the fluorine substitution at the para-position on the PEA organic cation can drastically improve the separation efficiency of photogenerated electron and hole and allow more efficient migration of charge carriers. Consequently, enhanced photocatalytic activity can be expected on bare 4-FPEA<sub>2</sub>PbI<sub>4</sub>.

We then conducted TA spectroscopy on Pt/perovskite to analyze the interfacial charge transfer dynamics from perovskite to Pt co-catalyst. Figure S17-S18 show the exciton bleach kinetics of the bare perovskites and Pt/perovskite samples. It can be observed that the exciton bleach kinetics of Pt/perovskite are significantly faster than those of bare perovskites. The exciton bleach kinetics of Pt/perovskite samples (Figure S19) were fitted using a bi-exponential decay model, and the fitting parameters are listed in Table S2. The average electron transfer time constants were determined to be ca. 87.2 ps for Pt/PEA<sub>2</sub>PbI<sub>4</sub> and ca. 14.8 ps for Pt/4-FPEA<sub>2</sub>PbI<sub>4</sub>. As Pt promotes the proton reduction reaction, the only difference between the kinetics of perovskite and Pt/perovskite is the electron transfer process from perovskite to Pt. By normalizing the exciton bleach kinetic tails of the perovskite and Pt/perovskite sample and subtracting them, we can exclude the contribution from the bare perovskite and obtain the kinetics of the electron transfer process from perovskite to Pt co-catalyst (Figure S20-S21). We employed a bi-exponential decay model to describe the interface electron transfer between perovskite and Pt co-catalyst, accounting for the heterogeneities in binding numbers and geometry of the electron transfer process (Fig. 5e). The obtained interfacial charge transfer efficiencies are 85.8% and 96.1% for Pt/PEA<sub>2</sub>PbI<sub>4</sub> and Pt/4-FPEA<sub>2</sub>PbI<sub>4</sub> samples, respectively (Table S3), according to which more efficient interfacial charge transfer between the perovskites and Pt co-catalyst can be achieved on Pt/4-FPEA<sub>2</sub>PbI<sub>4</sub>, enhancing photocatalytic hydrogen evolution activity.

After conducting PL, TRPL and TA measurements, we further employed Kelvin probe force microscope (KPFM) to measure the surface photovoltage (SPV) to probe the charge separation and transportation on the surface of the perovskite under light irradiation [73-76]. The KPFM image were measured with the surface potential change after light irradiation at a wavelength of 450 nm. Fig. 6a-h show the atomic force microscopy (AFM) images and the surface photovoltage microscopy (SPVM) images of the perovskite samples. The photogenerated electrons and holes were uniformly distributed on the whole perovskite surface. Moreover, bare 4-FPEA<sub>2</sub>PbI<sub>4</sub> exhibited a mean SPV of -11.4 mV, which

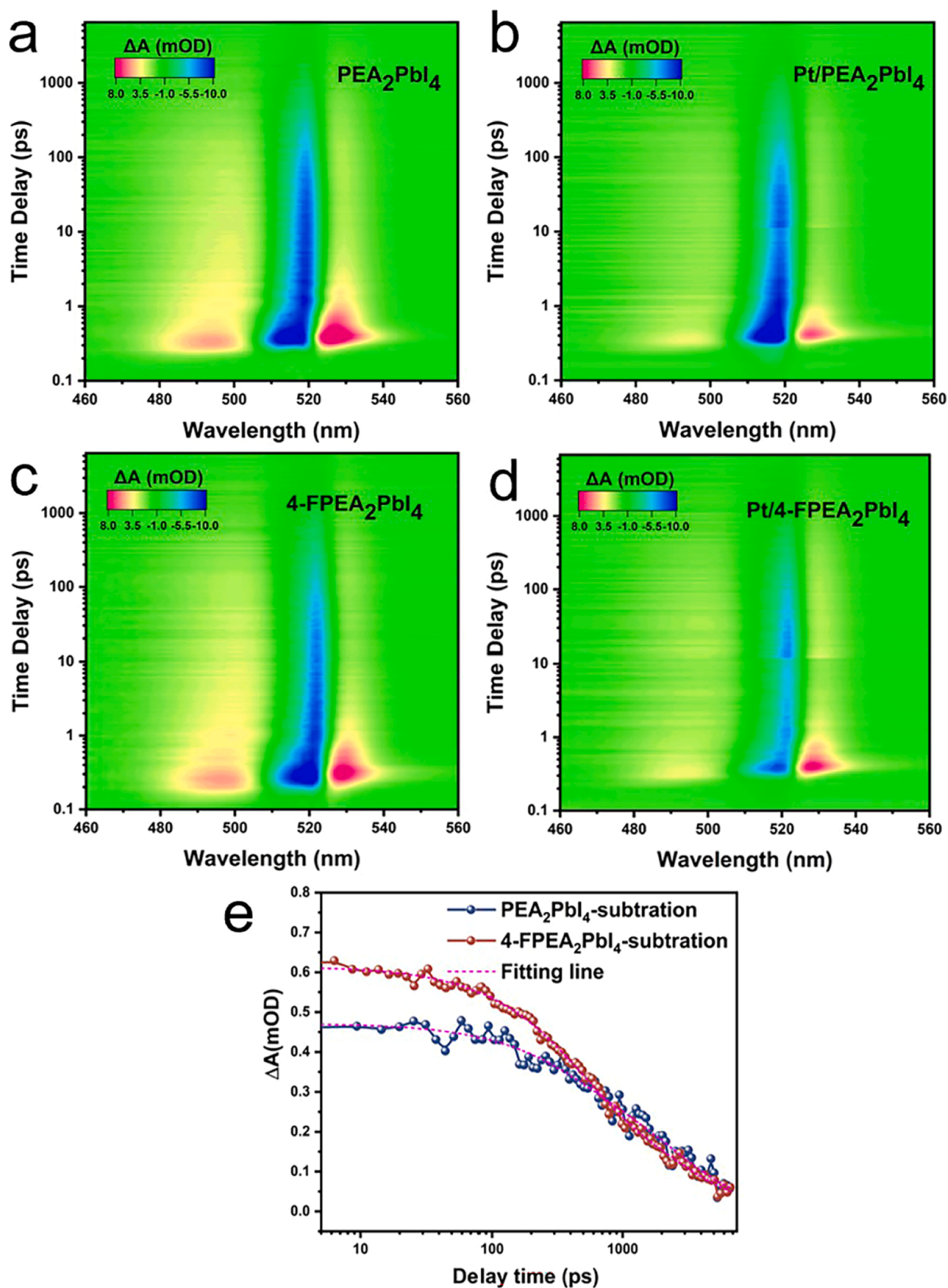
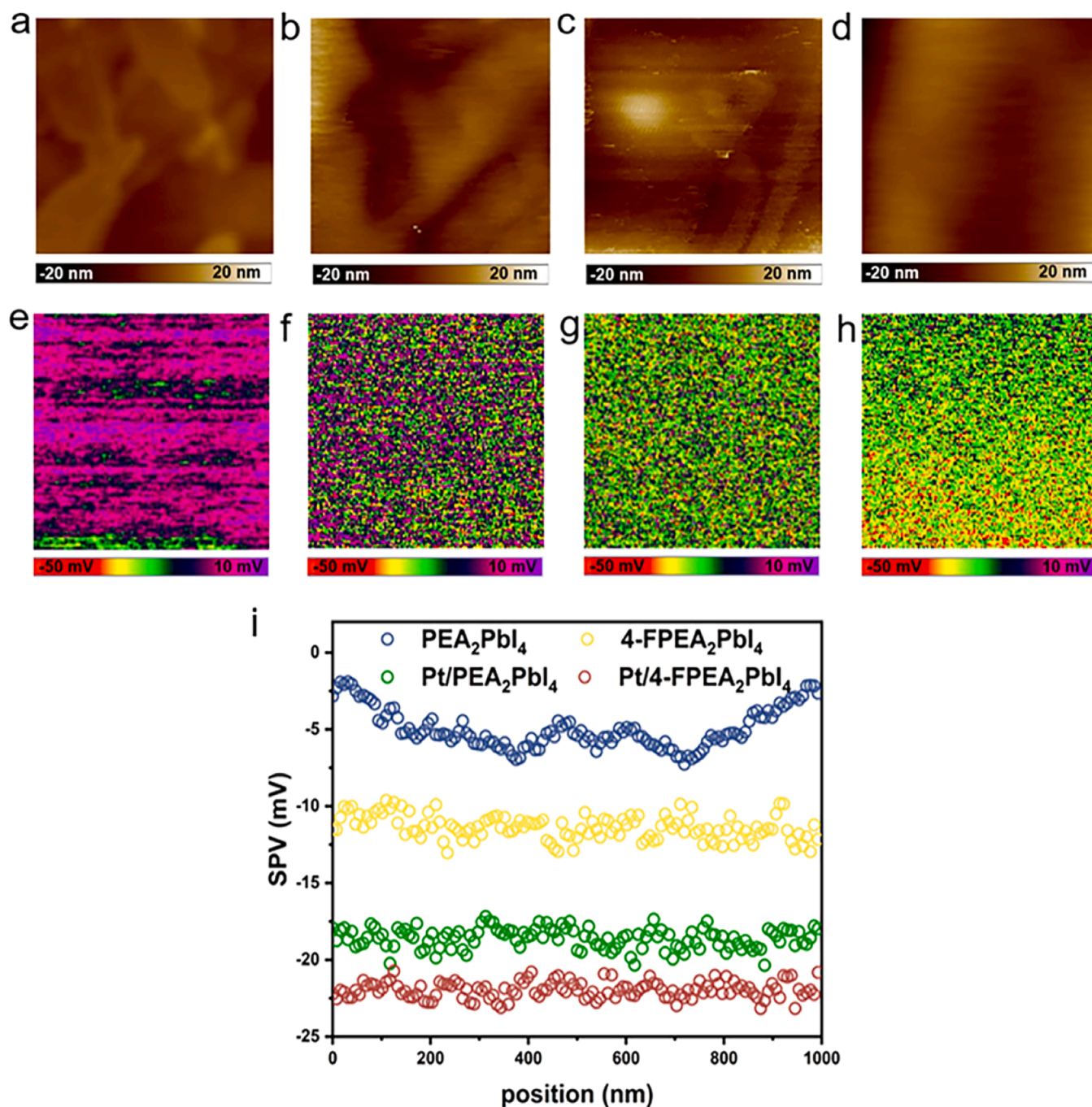


Fig. 5. Two-dimensional pseudo color plots of TA spectra at 400 nm excitation. (a)  $\text{PEA}_2\text{PbI}_4$ , (b)  $\text{Pt/PEA}_2\text{PbI}_4$ , (c)  $4\text{-FPEA}_2\text{PbI}_4$ , (d)  $\text{Pt/4-FPEA}_2\text{PbI}_4$ . (e) TA kinetics of the  $\text{PEA}_2\text{PbI}_4$   $4\text{-FPEA}_2\text{PbI}_4$  samples obtained by performing a subtraction between exciton bleach kinetics with perovskites and Pt/perovskites. The pink solid lines are bi-exponential decay model fit to the kinetics.





**Fig. 6.** AFM topography of the 2D perovskites. (a)  $\text{PEA}_2\text{PbI}_4$ , (b)  $\text{Pt}/\text{PEA}_2\text{PbI}_4$ , (c)  $4\text{-FPEA}_2\text{PbI}_4$ , (d)  $\text{Pt}/4\text{-FPEA}_2\text{PbI}_4$ . SPV distribution of perovskite samples. (e)  $\text{PEA}_2\text{PbI}_4$ , (f)  $\text{Pt}/\text{PEA}_2\text{PbI}_4$ , (g)  $4\text{-FPEA}_2\text{PbI}_4$ , (h)  $\text{Pt}/4\text{-FPEA}_2\text{PbI}_4$ . (i) Surface photovoltage of  $\text{PEA}_2\text{PbI}_4$ ,  $4\text{-FPEA}_2\text{PbI}_4$ ,  $\text{Pt}/\text{PEA}_2\text{PbI}_4$  and  $\text{Pt}/4\text{-FPEA}_2\text{PbI}_4$  by subtracting the potential under dark conditions from that under 450 nm illumination.

is much more negative than that obtained on bare  $\text{PEA}_2\text{PbI}_4$  (Fig. 6i and Table S4). This indicates that both perovskites are of p-type and more efficient electron transfer from the bulk to the surface can occur on  $4\text{-FPEA}_2\text{PbI}_4$  under light irradiation. As for  $\text{Pt}/\text{PEA}_2\text{PbI}_4$  and  $\text{Pt}/4\text{-FPEA}_2\text{PbI}_4$  perovskite samples, the mean SPV was further reduced to  $-18.6$  and  $-22$  mV, respectively, indicating that the presence of Pt co-catalyst can enable more efficient electron transfer to the surface. Therefore, the SPV analysis further demonstrated that rationally engineering the intercalated cation of 2D perovskite can modify the optoelectronic properties of the pristine perovskite and lead to more efficient charge transfer.

To gain more insight on why more efficient electron transfer occurs

for  $4\text{-FPEA}_2\text{PbI}_4$  compared with  $\text{PEA}_2\text{PbI}_4$ , density functional theory (DFT) calculations were performed. Fig. 7a and d show the optimized geometries for  $\text{PEA}_2\text{PbI}_4$  and  $4\text{-FPEA}_2\text{PbI}_4$ , respectively, in which the interlayer van der Waals (vdW) gap has been highlighted by red dash lines, with left and right layers being indicated as L and R. As determined by the nature of vdW interaction, electron density over such gap is remarkably lower than those dominated by chemical bonds. Consequently, large barrier is often presented for electron transfer over the vdW gap, under which photo-induced hot electrons can be hardly separated from left to right side along the direction vertical to the Pb-I-Pb plane. In the case of  $\text{PEA}_2\text{PbI}_4$ , the vdW gap is dominated by non-polarized interface between L and R layers, resulting in loose packing,



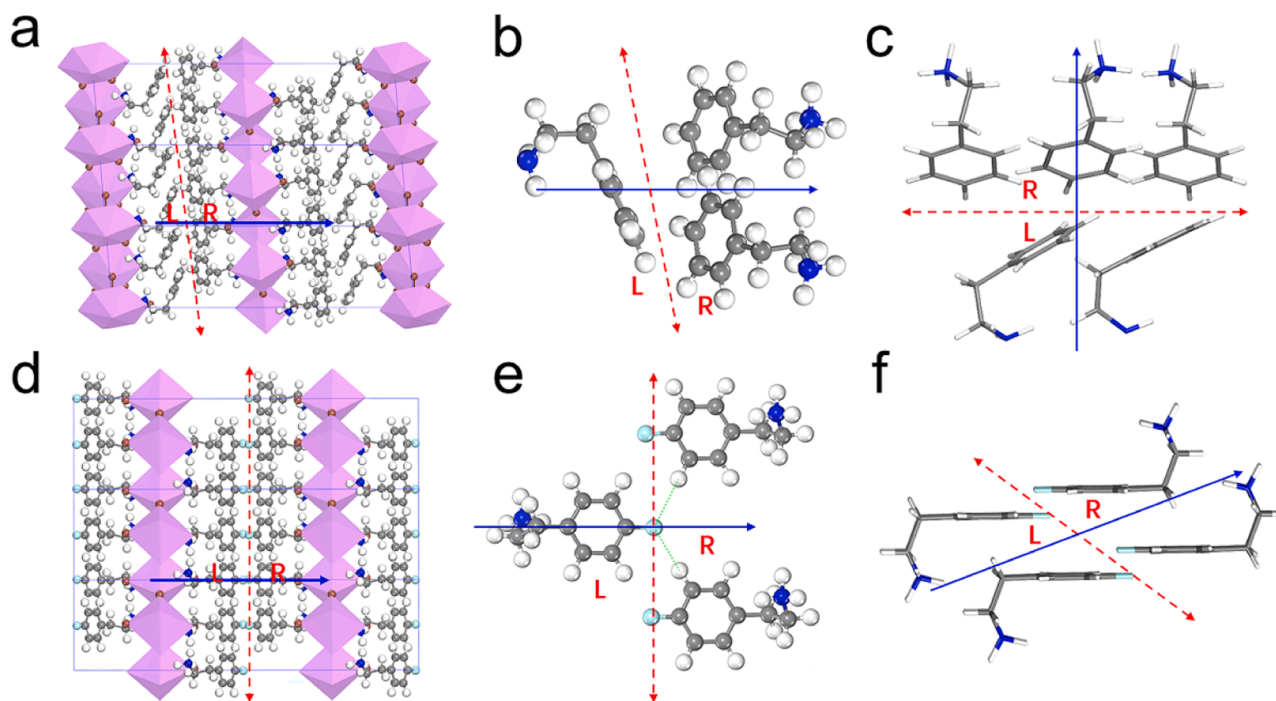


**Fig. 7.** The optimized geometries of  $\text{PEA}_2\text{PbI}_4$  and  $4\text{-FPEA}_2\text{PbI}_4$ . (a)-(c) for  $\text{PEA}_2\text{PbI}_4$  supercells and highlighted L-R vdW gap, (d)-(f) for  $4\text{-FPEA}_2\text{PbI}_4$ . Red dash lines show vdW gap, blue lines for the direction of electron transfer, Pb-I unit as pink octahedrons, organic ligands shown as ball-and-sticks or sticks with C, F, N and H as grey, grey, blue and white colours.

as shown in Fig. 7b-c. After fluorine terminations have been introduced in  $4\text{-FPEA}_2\text{PbI}_4$ , however, regular close packing has been observed and presented in Fig. 7e-f, from which F-H interaction and  $\pi$ - $\pi$  stacking can be achieved, both being beneficial to strengthen the interaction between the L and R layers.

Now we turn to explore how fluorine substitution can change the behavior of electron transfer, which is critical for the whole photocatalytic process. As shown in Fig. 8a-b, electron density has been plotted for  $\text{PEA}_2\text{PbI}_4$  and  $4\text{-FPEA}_2\text{PbI}_4$ , from which almost no electron distributed over the interlayer boundary as determined by non-polarized

vdW gap. As a result, a potential barrier of 0.29 eV is obtained for electron transfer over such gap as derived from electrostatic potential profile in Fig. 8c. In the case of  $4\text{-FPEA}_2\text{PbI}_4$ , F-H interaction has been found at the gap and almost zero-potential barrier has been presented as shown in Fig. 8d. Therefore, it is reasonable to speculate that the ultrafast interlayer electron transfer is due to the polarized interface between neighboring organic layers when fluorine has been introduced. Correspondingly, the ultrafast interlayer electron transfer will lead to more efficient internal electron charge transfer, significantly boosting the photocatalytic hydrogen evolution activity on  $4\text{-FPEA}_2\text{PbI}_4$ .

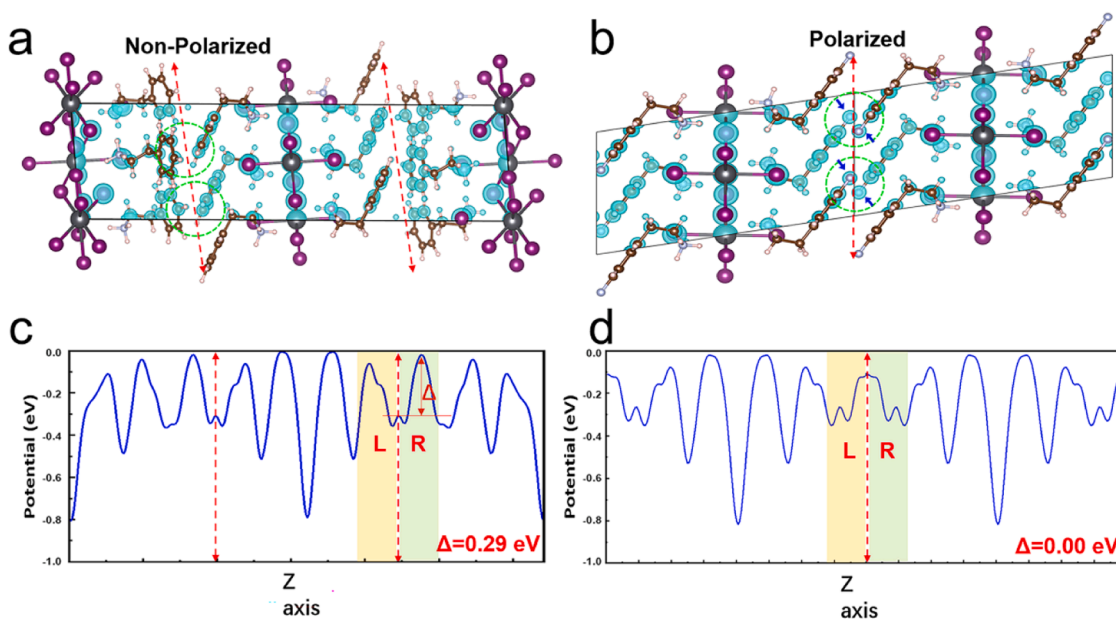


**Fig. 8.** Calculated electron density and electrostatic potential with (a) and (c) for  $\text{PEA}_2\text{PbI}_4$ , (b) and (d) for  $4\text{-FPEA}_2\text{PbI}_4$ . Potential difference ( $\Delta$ ) between organic link layers has been presented in c&d.

## 4. Conclusions

In summary, we demonstrated that rational engineering of the organic cations in 2D PEA<sub>2</sub>PbI<sub>4</sub> enabled more efficient internal electron transfer and thus led to drastically enhanced photocatalytic H<sub>2</sub> evolution activity. By substituting the hydrogen with fluorine atom in the para-position of the phenyl group of PEA<sub>2</sub>PbI<sub>4</sub>, internal electron transfer has been improved remarkably, which is ascribed to the interlayer polarization and substantially reduced energy barrier between the resulting organic layers. Consequently, 4-FPEA<sub>2</sub>PbI<sub>4</sub> exhibited ca. 8.2 times higher photocatalytic H<sub>2</sub> evolution activity than the parent PEA<sub>2</sub>PbI<sub>4</sub> together with excellent stability. This work not only highlights the importance of interlayer electron transfer for 2D perovskite but also sheds light on improving the photocatalytic properties of 2D perovskites by rationally engineering the intercalated organic cations.

## CRediT authorship contribution statement

**Xu Zong:** Writing – review & editing, Supervision, Funding acquisition. **Chenghua Sun:** Writing – review & editing, Supervision, Investigation. **Lianzhou Wang:** Writing – review & editing, Supervision. **Yuxin Xie:** Investigation. **Yuying Gao:** Investigation. **Hefeng Zhang:** Supervision. **Junhui Wang:** Investigation. **Jiaqi Liu:** Writing – original draft, Investigation.

## Declaration of Competing Interest

The authors declare that they have no known competing financial interests or personal relationships that could have appeared to influence the work reported in this paper.

## Data Availability

Data will be made available on request.

## Acknowledgements

This work was financially supported by National Natural Science Foundation of China (Grant No. 22179015, 21872142, 22302026), Liaoning Revitalization Talents Program (XLYC1807196).

## Appendix A. Supporting information

Supplementary data associated with this article can be found in the online version at [doi:10.1016/j.apcatb.2024.124018](https://doi.org/10.1016/j.apcatb.2024.124018).

## References

- J. Ran, J. Zhang, J. Yu, M. Jaroniec, S.Z. Qiao, Earth-abundant cocatalysts for semiconductor-based photocatalytic water splitting, *Chem. Soc. Rev.* 43 (2014) 7787–7812, <https://doi.org/10.1039/c3cs60425j>.
- T.P. Yoon, M.A. Ischay, J. Du, Visible light photocatalysis as a greener approach to photochemical synthesis, *Nat. Chem.* 2 (2010) 527–532, <https://doi.org/10.1038/nchem.687>.
- X. Zou, Y. Zhang, Noble metal-free hydrogen evolution catalysts for water splitting, *Chem. Soc. Rev.* 44 (2015) 5148–5180, <https://doi.org/10.1039/c4cs00448e>.
- X. Chen, S. Shen, L. Guo, S. Mao, Semiconductor-based photocatalytic hydrogen generation, *Chem. Rev.* 110 (2010) 6503–6570, <https://doi.org/10.1021/cr1001645>.
- S.Y. Reece, J.A. Hamel, K. Sung, T.D. Jarvi, A.J. Esswein, J.J. Pijpers, D.G. Nocera, Wireless solar water splitting using silicon-based semiconductors and earth-abundant catalysts, *Science* 334 (2011) 645–648, <https://doi.org/10.1126/science.1209816>.
- K. Maeda, K. Teramura, D. Lu, T. Takata, N. Saito, Y. Inoue, K. Domen, Photocatalyst releasing hydrogen from water, *Nature* 440 (2006) 295, <https://doi.org/10.1038/440295a>.
- W. Wang, G. Li, T. An, D.L. Chan, J.C. Yu, P.K. Wong, Photocatalytic hydrogen evolution and bacterial inactivation utilizing sonochemical-synthesized g-C<sub>3</sub>N<sub>4</sub>/red phosphorus hybrid nanosheets as a wide-spectral-responsive photocatalyst: The role of type I band alignment, *Appl. Catal. B-Environ.* 238 (2018) 126–135, <https://doi.org/10.1016/j.apcatb.2018.07.004>.
- W. Wang, T. An, G. Li, D. Xia, H. Zhao, J.C. Yu, P.K. Wong, Earth-abundant Ni<sub>2</sub>P/g-C<sub>3</sub>N<sub>4</sub> lamellar nanohybrids for enhanced photocatalytic hydrogen evolution and bacterial inactivation under visible light irradiation, *Appl. Catal. B-Environ.* 217 (2017) 570–580, <https://doi.org/10.1016/j.apcatb.2017.06.027>.
- S. Cao, Y. Chen, C. Wang, P. He, W. Fu, Highly efficient photocatalytic hydrogen evolution by nickel phosphide nanoparticles from aqueous solution, *Chem. Commun.* 50 (2014) 10427–10429, <https://doi.org/10.1039/c4cc05026f>.
- K.E. deKrafft, C. Wang, W. Lin, Metal-organic framework templated synthesis of Fe<sub>2</sub>O<sub>3</sub>/TiO<sub>2</sub> nanocomposite for hydrogen production, *Adv. Mater.* 24 (2012) 2014–2018, <https://doi.org/10.1002/adma.201200330>.
- J. Ng, S. Xu, X. Zhang, H. Yang, D.D. Sun, Hybridized Nanowires and Cubes: A Novel Architecture of a Heterojunctioned TiO<sub>2</sub>/SrTiO<sub>3</sub> Thin Film for Efficient Water Splitting, *Adv. Funct. Mater.* 20 (2010) 4287–4294, <https://doi.org/10.1002/adfm.201000931>.
- L. Chu, J. Zhang, W. Liu, R. Zhang, J. Yang, R. Hu, X. Li, W. Huang, A facile and green approach to synthesize mesoporous anatase TiO<sub>2</sub> nanomaterials for efficient dye-sensitized and hole-conductor-free perovskite solar cells, *ACS Sustain. Chem. En.* 6 (2018) 5588–5597, <https://doi.org/10.1021/acssuschemeng.8b00607>.
- L. Chu, W. Liu, Z. Qin, R. Zhang, R. Hu, J. Yang, J. Yang, X. Li, Boosting efficiency of hole conductor-free perovskite solar cells by incorporating p-type NiO nanoparticles into carbon electrodes, *Sol. Energy Mater. Sol. Cells* 178 (2018) 164–169, <https://doi.org/10.1016/j.solmat.2018.01.010>.
- L. Chu, W. Ahmad, W. Liu, J. Yang, R. Zhang, Y. Sun, J. Yang, X. Li, Lead-free halide double perovskite materials: a new superstar toward green and stable optoelectronic applications, *Nanomicro Lett.* 11 (2019) 16, <https://doi.org/10.1007/s40820-019-0244-6>.
- S. Park, W.J. Chang, C.W. Lee, S. Park, H.Y. Ahn, K.T. Nam, Photocatalytic hydrogen generation from hydriodic acid using methylammonium lead iodide in dynamic equilibrium with aqueous solution, *Nat. Energy* 2 (2016), <https://doi.org/10.1038/nenergy.2016.185>.
- Y. Guo, G. Liu, Z. Li, Y. Lou, J. Chen, Y. Zhao, Stable lead-free (CH<sub>3</sub>NH<sub>3</sub>)<sub>3</sub>Bi<sub>2</sub>I<sub>9</sub> perovskite for photocatalytic hydrogen generation, *ACS Sustain. Chem. En.* 7 (2019) 15080–15085, <https://doi.org/10.1021/acssuschemeng.9b03761>.
- H. Wang, X. Wang, R. Chen, H. Zhang, X. Wang, J. Wang, J. Zhang, L. Mu, K. Wu, F. Fan, X. Zong, C. Li, Promoting Photocatalytic H<sub>2</sub> Evolution on Organic-Inorganic Hybrid Perovskite Nanocrystals by Simultaneous Dual-Charge Transportation Modulation, *ACS Energy Lett.* 4 (2018) 40–47, <https://doi.org/10.1021/acscenergylett.8b01830>.
- Y. Wu, P. Wang, Z. Guan, J. Liu, Z. Wang, Z. Zheng, S. Jin, Y. Dai, M.-H. Whangbo, B. Huang, Enhancing the Photocatalytic Hydrogen Evolution Activity of Mixed-Halide Perovskite CH<sub>3</sub>NH<sub>3</sub>PbBr<sub>3-x</sub>I<sub>x</sub> Achieved by Bandgap Funneling of Charge Carriers, *ACS Catal.* 8 (2018) 10349–10357, <https://doi.org/10.1021/acscatal.8b02374>.
- X. Wang, H. Wang, H. Zhang, W. Yu, X. Wang, Y. Zhao, X. Zong, C. Li, Dynamic Interaction between Methylammonium Lead Iodide and TiO<sub>2</sub> Nanocrystals Leads to Enhanced Photocatalytic H<sub>2</sub> Evolution from HI Splitting, *ACS Energy Lett.* 3 (2018) 1159–1164, <https://doi.org/10.1021/acscenergylett.8b00488>.
- Y. Wu, P. Wang, X. Zhu, Q. Zhang, Z. Wang, Y. Liu, G. Zou, Y. Dai, M.H. Whangbo, B. Huang, Composite of CH<sub>3</sub>NH<sub>3</sub>PbI<sub>3</sub> with reduced graphene oxide as a highly efficient and stable visible-light photocatalyst for hydrogen evolution in aqueous HI solution, *Adv. Mater.* 30 (2018) 1704342, <https://doi.org/10.1002/adma.201704342>.
- Z. Zhao, J. Wu, Y.-Z. Zheng, N. Li, X. Li, X. Tao, Ni<sub>3</sub>C-decorated MAPbI<sub>3</sub> as visible-light photocatalyst for H<sub>2</sub> evolution from HI splitting, *ACS Catal.* 9 (2019) 8144–8152, <https://doi.org/10.1021/acscatal.9b01605>.
- X. Zhao, S. Chen, H. Yin, S. Jiang, K. Zhao, J. Kang, P. Liu, L. Jiang, Z. Zhu, D. Cui, P. Liu, X. Han, H. Yang, H. Zhao, Perovskite microcrystals with intercalated monolayer MoS<sub>2</sub> nanosheets as advanced photocatalyst for solar-powered hydrogen generation, *Matter* 3 (2020) 935–949, <https://doi.org/10.1016/j.matt.2020.07.004>.
- F. Wang, X. Liu, Z. Zhang, S. Min, A noble-metal-free MoS<sub>2</sub> nanosheet-coupled MAPbI<sub>3</sub> photocatalyst for efficient and stable visible-light-driven hydrogen evolution, *Chem. Commun.* 56 (2020) 3281–3284, <https://doi.org/10.1039/d0cc00095g>.
- X. Liu, Q. Zhang, S. Zhao, Z. Wang, Y. Liu, Z. Zheng, H. Cheng, Y. Dai, B. Huang, P. Wang, Integrating Mixed Halide Perovskite Photocatalytic HI Splitting and Electrocatalysis into a Loop for Efficient and Robust Pure Water Splitting, *Adv. Mater.* 35 (2023) 2208915, <https://doi.org/10.1002/adma.202208915>.
- H. Li, X. Lv, R. Li, X. Tao, Y. Zheng, Stable and efficient Ti<sub>3</sub>C<sub>2</sub> MXene/MAPbI<sub>3</sub>-HI system for visible-light-driven photocatalytic HI splitting, *J. Power Sources* 522 (2022) 231006, <https://doi.org/10.1016/j.jpowsour.2022.231006>.
- C. Cai, Y. Teng, J. Wu, J. Li, H. Chen, J. Chen, D. Kuang, Situ photosynthesis of an MAPbI<sub>3</sub>/CoP hybrid heterojunction for efficient photocatalytic hydrogen evolution, *Adv. Funct. Mater.* 30 (2020) 22201478, <https://doi.org/10.1016/j.adfm.202001478>.
- Y. Wu, Q. Wu, Q. Zhang, Z. Lou, K. Liu, Y. Ma, Z. Wang, Z. Zheng, H. Cheng, Y. Liu, Y. Dai, B. Huang, P. Wang, An organometal halide perovskite supported Pt single-atom photocatalyst for H<sub>2</sub> evolution, *Energy Environ. Sci.* 15 (2022) 1271–1281, <https://doi.org/10.1039/d1ee03679c>.
- H. Wang, H. Zhang, J. Wang, Y. Gao, F. Fan, K. Wu, X. Zong, C. Li, Mechanistic understanding of efficient photocatalytic H<sub>2</sub> evolution on two-dimensional layered lead iodide hybrid perovskites, *Angew. Chem. Int. Ed.* 60 (2021) 7376–7381, <https://doi.org/10.1002/anie.202014623>.
- I.C. Smith, E.T. Hoke, D. Solis-Ibarra, M.D. McGehee, H.I. Karunadasa, A layered hybrid perovskite solar-cell absorber with enhanced moisture stability, *Angew. Chem. Int. Ed.* 53 (2014) 11232–11235, <https://doi.org/10.1002/anie.201406466>.

- [30] Y. Zhou, F. Wang, Y. Cao, J. Wang, H. Fang, M. Loi, N. Zhao, C. Wong, Benzylamine-treated wide-bandgap perovskite with high thermal-photostability and photovoltaic performance, *Adv. Energy Mater.* 7 (2017) 1701048, <https://doi.org/10.1002/aenm.201701048>.
- [31] Y. Lin, Y. Bai, Y. Fang, Q. Wang, Y. Deng, J. Huang, Suppressed Ion Migration in Low-Dimensional Perovskites, *ACS Energy Lett.* 2 (2017) 1571–1572, <https://doi.org/10.1021/acsenrgylett.7b00442>.
- [32] D. Li, K. Wang, J. Tang, Y. Zhao, H. Elhaes, M. Tahir, M.A. Ibrahim, Y. Li, Efficient photosensitized singlet oxygen generation in two-dimensional perovskite nanosheets via energy transfer, *Appl. Surf. Sci.* 613 (2023) 155911, <https://doi.org/10.1016/j.apsusc.2022.155991>.
- [33] A. Fakharuddin, M.K. Gangishetty, M. Abdi-Jalebi, S.H. Chin, A.B. Yusoff, D. N. Congreve, W. Tress, F. Deschler, M. Vasilopoulou, H.J. Bolink, Perovskite light-emitting diodes, *Nat. Electron.* 5 (2022) 203–216, <https://doi.org/10.1038/s41928-022-00745-7>.
- [34] N. Li, X. Niu, Q. Chen, H. Zhou, Towards commercialization: the operational stability of perovskite solar cells, *Chem. Soc. Rev.* 49 (2020) 8235–8286, <https://doi.org/10.1039/d0cs00573h>.
- [35] S. Park, W.J. Chang, C.W. Lee, S. Park, H.Y. Ahn, K.T. Nam, Photocatalytic hydrogen generation from hydriodic acid using methylammonium lead iodide in dynamic equilibrium with aqueous solution, *Nat. Energy* 2 (2017) 16185, <https://doi.org/10.1038/nenergy.2016.185>.
- [36] Y. Xu, M. Yang, B. Chen, X. Wang, H. Chen, D. Kuang, C. Su, A CsPbBr<sub>3</sub> perovskite quantum dot/graphene oxide composite for photocatalytic CO<sub>2</sub> reduction, *J. Am. Chem. Soc.* 139 (2017) 5660–5663, <https://doi.org/10.1021/jacs.7b00489>.
- [37] C.C. Stoumpos, D.H. Cao, D.J. Clark, J. Young, J.M. Rondinelli, J.L. Jang, J. T. Hupp, M.G. Kanatzidis, Ruddlesden-popper hybrid lead iodide perovskite 2D homologous semiconductors, *Chem. Mater.* 28 (2016) 2852–2867, <https://doi.org/10.1021/acs.chemmater.6b00847>.
- [38] X. Li, J.M. Hoffman, M.G. Kanatzidis, The 2D halide perovskite rulebook: how the spacer influences everything from the structure to optoelectronic device efficiency, *Chem. Rev.* 121 (2021) 2230–2291, <https://doi.org/10.1021/acs.chemrev.0c01006>.
- [39] S. Ghimire, C. Klinker, Two-dimensional halide perovskites: synthesis, optoelectronic properties, stability, and applications, *Nanoscale* 13 (2021) 12394–12422, <https://doi.org/10.1039/d1nr02769g>.
- [40] B. Saparov, D.B. Mitzi, Organic-inorganic perovskites: structural versatility for functional materials design, *Chem. Rev.* 116 (2016) 4558–4596, <https://doi.org/10.1021/acs.chemrev.5b00715>.
- [41] H. Pan, X. Zhao, X. Gong, Y. Shen, M. Wang, Atomic-scale tailoring of organic cation of layered ruddlesden-popper perovskite compounds, *J. Phys. Chem. Lett.* 10 (2019) 1813–1819, <https://doi.org/10.1021/acs.jpclett.9b00479>.
- [42] W. Fu, H. Liu, X. Shi, D. Zuo, X. Li, L.K.Y. Jen, Tailoring the functionality of organic spacer cations for efficient and stable Quasi-2D perovskite solar cells, *Adv. Funct. Mater.* 29 (2019) 1900221, <https://doi.org/10.1002/adfm.201900221>.
- [43] J. Hu, I.W.H. Oswald, S.J. Stuart, M.M. Nahid, N. Zhou, O.F. Williams, Z. Guo, L. Yan, H. Hu, Z. Chen, X. Xiao, Y. Lin, Z. Yang, J. Huang, A.M. Moran, H. Ade, J. R. Neilson, W. You, Synthetic control over orientational degeneracy of spacer cations enhances solar cell efficiency in two-dimensional perovskites, *Nat. Commun.* 10 (2019) 1276, <https://doi.org/10.1038/s41467-019-08980-x>.
- [44] J.C. Jia, G.H. Liu, T. Jia, Z.F. Wang, K.W. Lin, Y. Li, F. Huang, Y. Cao, Fused nonacyclic electron acceptors with additional alkyl side chains for efficient polymer solar cells, *Org. Electron.* 68 (2019) 151–158, <https://doi.org/10.1016/j.orgel.2019.01.052>.
- [45] X. Li, J. Yao, I. Angunawala, C. Sun, L. Xue, A. Liebman-Pelaez, C. Zhu, C. Yang, Z. Zhang, H. Ade, Y. Li, Improvement of photovoltaic performance of polymer solar cells by rational molecular optimization of organic molecule acceptors, *Adv. Energy Mater.* 8 (2018) 1800815, <https://doi.org/10.1002/aenm.201800815>.
- [46] D. Bi, P. Gao, R. Scopelliti, E. Oveisi, J. Luo, M. Gratzel, A. Hagfeldt, M. K. Nazeeruddin, High-performance perovskite solar cells with enhanced environmental stability based on amphiphile-modified CH<sub>3</sub>NH<sub>3</sub>PbI<sub>3</sub>, *Adv. Mater.* 28 (2016) 2910–2915, <https://doi.org/10.1002/adma.201505255>.
- [47] A. Mondal, T. Alam, M. Khan, S. Gupta, Layered 2D perovskite (FPEA)<sub>2</sub>PbI<sub>4</sub> as moisture tolerant photocatalyst compared to 3D MAPbI<sub>3</sub>, *Mater. Lett.* 331 (2023) 133519, <https://doi.org/10.1016/j.matlet.2022.133519>.
- [48] K. Chondroudis, D.B. Mitzi, P. Brock, Effect of Thermal Annealing on the Optical and Morphological Properties of (AETH)PbX<sub>4</sub> (X = Br, I) perovskite films prepared using single source thermal ablation, *Chem. Mater.* 12 (1999) 169–175, <https://doi.org/10.1021/cm990516l>.
- [49] C. Lermer, S.T. Birkhold, I.L. Moudrakovski, P. Mayer, L.M. Schoop, L. Schmidt-Mende, B.V. Lotsch, Toward fluorinated spacers for MAPI-derived hybrid perovskites: synthesis, characterization, and phase transitions of (FC<sub>2</sub>H<sub>4</sub>NH<sub>3</sub>)<sub>2</sub>PbCl<sub>4</sub>, *Chem. Mater.* 28 (2016) 6560–6566, <https://doi.org/10.1021/acs.chemmater.6b02151>.
- [50] Z. Wang, Q. Wei, X. Liu, L. Liu, X. Tang, J. Guo, S. Ren, G. Xing, D. Zhao, Y. Zheng, Spacer cation tuning enables vertically oriented and graded Quasi-2D perovskites for efficient solar cells, *Adv. Funct. Mater.* 31 (2020) 2008404, <https://doi.org/10.1002/adfm.202008404>.
- [51] F. Zhang, D.H. Kim, H. Lu, J.-S. Park, B.W. Larson, J. Hu, L. Gao, C. Xiao, O.G. Reid, X. Chen, Q. Zhao, P.F. Ndione, J.J. Berry, W. You, A. Walsh, M.C. Beard, K. Zhu, Enhanced charge transport in 2D perovskites via fluorination of organic cation, *J. Am. Chem. Soc.* 141 (2019) 5972–5979, <https://doi.org/10.1021/jacs.9b00972>.
- [52] M. Worku, A. Ben-Akacha, S. Sridhar, J.R. Frick, S.C. Yin, Q.Q. He, A.J. Robb, M. Chaaban, H. Liu, J.S.R.V. Winfred, K. Hanson, F. So, D. Dougherty, B.W. Ma, Band Edge Control of Quasi-2D metal halide perovskites for blue light-emitting diodes with enhanced performance, *Adv. Funct. Mater.* 31 (2021) 2103299, <https://doi.org/10.1002/adfm.202103299>.
- [53] J. Shi, Y. Gao, X. Gao, Y. Zhang, J. Zhang, X. Jing, M. Shao, Fluorinated low-dimensional ruddlesden-popper perovskite solar cells with over 17% power conversion efficiency and improved stability, *Adv. Mater.* 31 (2019) e1901673, <https://doi.org/10.1002/adma.201901673>.
- [54] K. Kikuchi, Y. Takeoka, M. Rikukawa, K. Sanui, Structure and optical properties of lead iodide based two-dimensional perovskite compounds containing fluorophenethylamines, *Curr. Appl. Phys.* 4 (2004) 599–602, <https://doi.org/10.1016/j.cap.2004.01.027>.
- [55] D.B. Mitzi, C.D. Dimitrakopoulos, L.L. Kosbar, Structurally tailored organic-inorganic perovskites: optical properties and solution-processed channel materials for thin-film transistors, *Chem. Mater.* 13 (2001) 3728–3740, <https://doi.org/10.1021/cm010105g>.
- [56] Y. Guo, G. Liu, Z. Li, Y. Lou, J. Chen, Y. Zhao, Stable Lead-Free (CH<sub>3</sub>NH<sub>3</sub>)<sub>3</sub>BiI<sub>9</sub> Perovskite for Photocatalytic Hydrogen Generation, *ACS Sustain. Chem. Eng.* 7 (2019) 15080–15085, <https://doi.org/10.1021/acssuschemeng.9b03761>.
- [57] S.A. Penkett, A.W. Adamson, Flash Photolysis of Cobalt(III) Acidopentaammine and of PtBr<sub>6</sub><sup>2-</sup> and PtI<sub>6</sub><sup>2-</sup> Complexes, *J. Am. Chem. Soc.* 87 (1965) 2514–2515, <https://doi.org/10.1021/JA01089A052>.
- [58] J. Ma, X. Tan, Q. Zhang, Y. Wang, J. Zhang, L. Wang, Exploring the Size Effect of Pt Nanoparticles on the Photocatalytic Nonoxidative Coupling of Methane, *ACS Catal.* 11 (2021) 3352–3360, <https://doi.org/10.1021/acscatal.0c04943>.
- [59] Y. Dong, C. Lian, C. Hu, Z.S. Deng, J.-Q. Gong, M.D. Li, H.L. Liu, M.Y. Xing, J. L. Zhang, Size-dependent activity and selectivity of carbon dioxide photocatalytic reduction over platinum nanoparticles, *Nat. Commun.* 9 (2018) 1252, <https://doi.org/10.1038/s41467-018-03666-2>.
- [60] R. Kuriki, H. Matsunaga, T. Nakashima, K. Wada, A. Yamakata, O. Ishitani, K. Maeda, Nature-Inspired, Highly Durable CO<sub>2</sub> Reduction System Consisting of a Binuclear Ruthenium(II) Complex and an Organic Semiconductor Using Visible Light, *J. Am. Chem. Soc.* 138 (2016) 5159–5170, <https://doi.org/10.1021/jacs.6b01997>.
- [61] S. Min, G. Lu, Dye-cosensitized graphene/Pt photocatalyst for high efficient visible light hydrogen evolution, *Int. J. Hydrog. Energ.* 37 (2012) 10564–10574, <https://doi.org/10.1016/j.ijhydene.2012.04.072>.
- [62] B. Ma, H. Xu, K. Lin, J. Li, H. Zhan, W. Liu, C. Li, Mo<sub>2</sub>C as Non-Noble Metal Co-Catalyst in Mo<sub>2</sub>C/CdS composite for enhanced photocatalytic H<sub>2</sub> evolution under visible light irradiation, *ChemSusChem* 9 (2016) 820–824, <https://doi.org/10.1002/cssc.201501652>.
- [63] Y. Qi, J. Zhang, Y. Kong, Y. Zhao, S. Chen, D. Li, W. Liu, Y. Chen, T. Xie, J. Cui, C. Li, K. Domen, F. Zhang, Unraveling of cocatalysts photodeposited selectively on facets of BiVO<sub>4</sub> to boost solar water splitting, *Nat. Commun.* 13 (2022) 484, <https://doi.org/10.1038/s41467-022-28146-6>.
- [64] Q. Ding, T. Chen, Z. Li, Z. Feng, X. Wang, Time-resolved infrared spectroscopic investigation of Ga<sub>2</sub>O<sub>3</sub> photocatalysts loaded with Cr<sub>2</sub>O<sub>3</sub>-Rh cocatalysts for photocatalytic water splitting, *Chin. J. Catal.* 42 (2021) 808–816, [https://doi.org/10.1016/S1872-2067\(20\)63688-9](https://doi.org/10.1016/S1872-2067(20)63688-9).
- [65] M. Matsuoka, M. Kitano, M. Takeuchi, K. Tsujimaru, M. Anpo, J.M. Thomas, Photocatalysis for new energy production—Recent advances in photocatalytic water splitting reactions for hydrogen production, *Catal. Today* 122 (2007) 51–61, <https://doi.org/10.1016/j.cattod.2007.01.042>.
- [66] M. Liu, W. You, Z. Lei, G. Zhou, J. Yang, G. Wu, G. Ma, G. Luan, T. Takata, M. Hara, K. Domen, C. Li, Water reduction and oxidation on Pt-Rh/Y<sub>2</sub>Ta<sub>2</sub>O<sub>7</sub>N<sub>2</sub> catalyst under visible light irradiation, *Chem. Commun.* (2004) 2192–2193, <https://doi.org/10.1039/b407892f>.
- [67] X. Zong, H. Yan, G. Wu, G. Ma, F. Wen, L. Wang, C. Li, Enhancement of Photocatalytic H<sub>2</sub> Evolution on CdS by Loading MoS<sub>2</sub> as Cocatalyst under Visible Light Irradiation, *J. Am. Chem. Soc.* 130 (2008) 7176–7177, <https://doi.org/10.1021/ja8007825>.
- [68] T. Wang, X. Li, Z. Qin, T. Wang, Y. Zhao, Activating photocatalytic hydrogen generation on inorganic lead-free Cs<sub>2</sub>AgBiBr<sub>6</sub> perovskite via reversible Cu<sup>+</sup>/Cu<sup>2+</sup> redox couple, *J. Catal.* 413 (2022) 509–516, <https://doi.org/10.1016/j.jcat.2022.07.009>.
- [69] C.H. Chuang, P.R. Brown, V. Bulovic, M.G. Bawendi, Improved performance and stability in quantum dot solar cells through band alignment engineering, *Nat. Mater.* 13 (2014) 796–801, <https://doi.org/10.1038/nmat3984>.
- [70] J. Liu, Y. Liu, N. Liu, Y. Han, X. Zhang, H. Huang, Y. Lifshitz, S.T. Lee, J. Zhong, Z. Kang, Water splitting. Metal-free efficient photocatalyst for stable visible water splitting via a two-electron pathway, *Science* 347 (2015) 970–974, <https://doi.org/10.1126/science.1258145>.
- [71] Z. Cui, Y. Wu, S. Zhang, H. Fu, G. Chen, Z. Lou, X. Liu, Q. Zhang, Z. Wang, Z. Zheng, H. Cheng, Y. Liu, Y. Dai, B. Huang, P. Wang, Insight into a strategy to improve charge carrier migration in lead-free bismuth-based halide perovskite for efficient selective oxidation of thioanisole under visible light, *Chem. Eng. J.* 451 (2023) 138927, <https://doi.org/10.1016/j.cej.2022.138927>.
- [72] H. Fu, X. Liu, J. Fu, Y. Wu, Q. Zhang, Z. Wang, Y. Liu, Z. Zheng, H. Cheng, Y. Dai, B. Huang, P. Wang, 2D/Quasi-2D ruddlesden-popper perovskite: a high-performance photocatalyst for hydrogen evolution, *ACS Catal.* 13 (2023) 14716–14724, <https://doi.org/10.1021/acscatal.3c03933>.
- [73] Y. Gao, J. Zhu, H. An, P. Yan, B. Huang, R. Chen, F. Fan, C. Li, Directly probing charge separation at interface of TiO<sub>2</sub> phase junction, *J. Phys. Chem. Lett.* 8 (2017) 1419–1423, <https://doi.org/10.1021/acs.jpclett.7b00285>.

- [74] R. Chen, S. Pang, H. An, J. Zhu, S. Ye, Y. Gao, F. Fan, C. Li, Charge separation via asymmetric illumination in photocatalytic  $\text{Cu}_2\text{O}$  particles, *Nat. Energy* 3 (2018) 655–663, <https://doi.org/10.1038/s41560-018-0194-0>.
- [75] J. Zhu, F. Fan, R. Chen, H. An, Z. Feng, C. Li, Direct imaging of highly anisotropic photogenerated charge separations on different facets of a single  $\text{BiVO}_4$  photocatalyst, *Angew. Chem. Int. Ed.* 54 (2015) 9111–9114, <https://doi.org/10.1002/anie.201504135>.
- [76] R. Li, F. Zhang, D. Wang, J. Yang, M. Li, J. Zhu, X. Zhou, H. Han, C. Li, Spatial separation of photogenerated electrons and holes among {010} and {110} crystal facets of  $\text{BiVO}_4$ , *Nat. Commun.* 4 (2013) 1432, <https://doi.org/10.1038/ncomms2401>.